Facile Synthesis and Intraparticle Self-Catalytic Oxidation of Dextran-Coated Hollow Au–Ag Nanoshell and Its Application for Chemo-Thermotherapy

Hongje Jang, Young-Kwan Kim, Hyun Huh, and Dal-Hee Min*

Center for RNA Research, Institute for Basic Science, Department of Chemistry, Seoul National University, Seoul 151-747, Republic of Korea

ABSTRACT Galvanic replacement reaction is a useful method to prepare various hollow nanostructures. We developed fast and facile preparation of biocompatible and structurally robust hollow Au–Ag nanostructures by using dextran-coated Ag nanoparticles. Oxidation of the surface dextran alcohols was enabled by catalytic activity of the core Au–Ag nanostructure, introducing carbonyl groups that are useful for further bioconjugation. Subsequent doxorubicin (Dox) conjugation *via* Schiff base formation was achieved, giving high payload of approximately 35 000 Dox per particle. Near-infrared-mediated photothermal conversion showed high efficacy of the Dox-loaded Au–Ag nanoshell as a combinational chemo-thermotherapy to treat cancer cells.

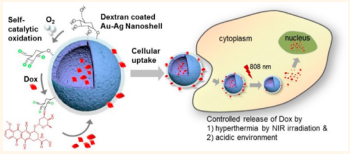

KEYWORDS: cancer · dextran · doxorubicin · hollow nanoparticle · photothermal therapy

Hollow gold nanostructures have been extensively investigated for applications in biosensing,[1,2] imaging,[3,4] catalysis,[5,6] and hyperthermia[7−9] due to their unique physicochemical properties including reduced density with nanoscale size, interior vacancy, high surface-to-volume ratio, strong surface plasmon resonance (SPR),[10−13] and photothermal effect.[14,15] Among them, photothermal effect is attractive for therapeutic applications such as a cancer treatment modality by inducing hyperthermia. A strong plasmon absorption band in the near-infrared (NIR) wavelength of hollow gold nanostructures can induce direct damage to the cells treated with the nanostructures by hyperthermia.[16−18] NIR irradiation is ideal for *in vivo* photothermal applications due to its low absorption by tissue chromophores including hemoglobin, thus allowing deep tissue penetration.[19−21] One approach for cancer therapy combines modalities of hyperthermia and chemotherapy, so-called chemo-thermotherapy, in which hyperthermia is used at a sublethal level to potentiate the therapeutic effect of anticancer agents. Another key feature of hollow gold nanostructures is catalytic activity which accelerates oxidative processes. First notable demonstration was reported on oxidation of CO to CO_2 by gold nanoclusters in 1989.[22] In principle, the high electric potential (E^0 = +1.69 V) of gold provides high material stability against catalytic poisoning against oxygen and other functional groups during the catalytic reaction.[23] Also, the high surface-to-volume ratio of gold nanomaterial—even higher in hollow structures—enables effective turnover rate in catalytic reactions. Selective oxidation property of gold nanomaterial in both gas and liquid phase can endow bulk-scale reaction with low activation energy, which is especially useful for industrial application.[24] Oxidation of alcohols,[25−27] diols,[28] polyols,[29] and carbohydrates[30] by gold nanoclusters provides an opportunity for integrating the relevant chemical modification with the conjugation of biomolecules for various biological applications.

Preparation of hollow gold nanostructures through galvanic replacement reaction was first reported by Xia and co-workers.[31] They employed galvanic replacement reaction which proceeds *via* oxidation of suspending silver nanostructures by $AuCl_4^-$ ions due to the standard reduction potential difference (Ag^+|Ag pair: 0.7996 V *vs* SHE, $AuCl_4^-$|Au pair: 0.93 V *vs* SHE) in an aqueous solution. Unlike other hollow nanostructure formation

* Address correspondence to dalheemin@snu.ac.kr.

Received for review September 16, 2013 and accepted January 2, 2014.

Published online January 02, 2014
10.1021/nn404833b

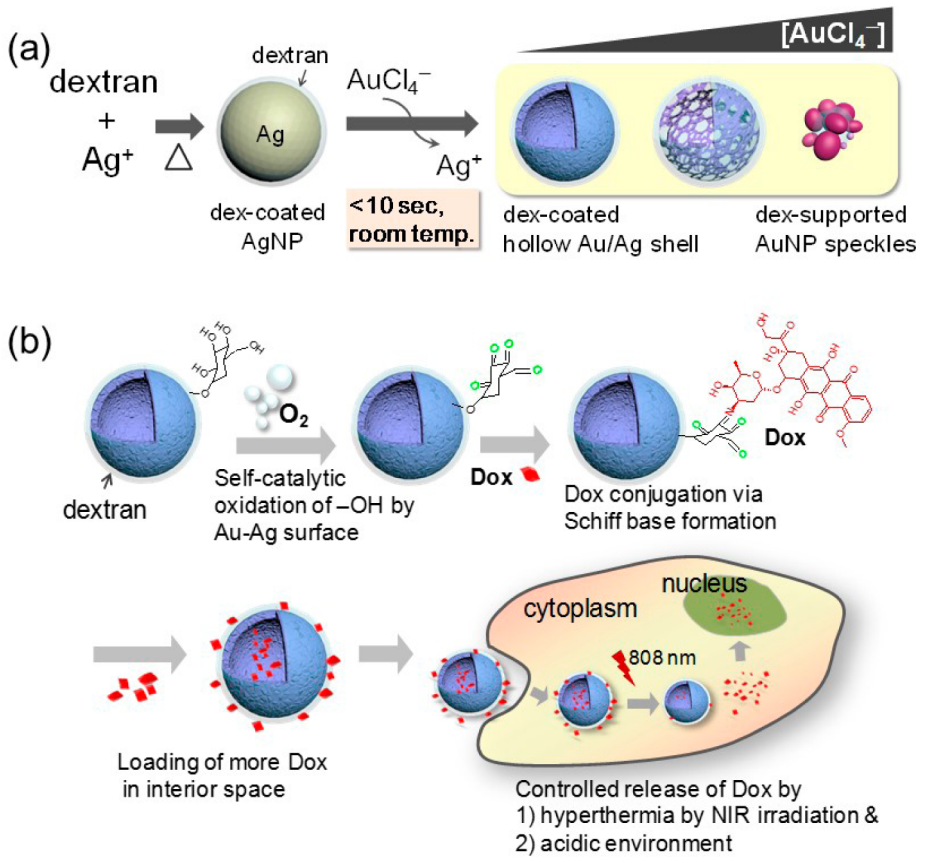

Figure 1. (a) Synthesis of dextran-coated hollow Au–Ag nanoparticles (dHANs) from dAgNPs by galvanic replacement reaction. Addition of small amount of $AuCl_4^-$ generates hollow Ag/Au alloy nanostructure, and addition of a higher concentration of $AuCl_4^-$ leads to porous structure. Even more excess $AuCl_4^-$ ions lead to structure deformation, resulting in irregular spherical structure. (b) Au–Ag core nanoparticle surface-mediated self-catalytic intraparticle alcohol oxidation of dextran coating, giving aldehyde and ketone moieties. The carbonyl functional groups were used to conjugate amine-containing molecules, Dox in the present study, through imine bond (Schiff base) formation. The Dox-loaded dHANs were readily endocytosed and showed high efficacy as a chemo-thermotherapy to treat cancer cells.

methods, such as template-mediated core–shell formation including silica or polymer latexes followed by etching,[32,33] nanoscale self-assembly of gold,[34] and layer-by-layer adsorption of polyelectrolytes and charged gold colloids,[35,36] galvanic replacement-mediated hollow gold shell formation offers many advantages such as simplicity of one-pot reaction, formation of homogeneous and highly crystalline structure, and no necessity for cytotoxic surfactant such as cetyl trimethylammonium bromide (CTAB) in synthetic procedures.[37]

Here, we prepared dextran-coated silver nanoparticle (dAgNP) as a precursor and carried out galvanic replacement reaction at room temperature with dAgNP to synthesize dextran-coated hollow Au–Ag bimetallic nanostructures (dHANs). Dextran is a biocompatible, highly branched polysaccharide polymer, which served as a reducing agent and surface coating at the same time for the AgNP preparation. In subsequent galvanic replacement reaction, dextran played a role to prevent structural collapse or agglomeration of the formed Au–Ag bimetallic hollow shell. Notably, the galvanic replacement reaction was completed within 10 s at room temperature, which is a considerably mild condition and short time compared to conventional methods which typically require high temperature of 100 °C with refluxing and/or long incubation time of several hours.[38] Additionally, in our dHANs, hydroxyl groups of dextran near the metal nanoparticle surface are readily oxidized to carbonyl groups by the catalytic activity of the Au–Ag nanostructure in a way similar to the previously reported examples on catalytic oxidation of diols and glucose. The resulting carbonyl groups serve as molecular handles to conjugate amine-containing molecules, giving Schiff base imine linkage. We finally demonstrated high efficacy of the doxorubicin (Dox)-loaded dHANs as a chemo-thermotherapeutics to cancer cells (HeLa, cervical cancer cell line), which showed NIR-triggered controlled release of Dox in cell cytoplasm.

RESULTS AND DISCUSSION

First, dAgNPs were prepared by a previously reported method that was established for dextran-coated gold nanoparticles (dAuNPs) by our group with slight modification.[39] Galvanic replacement reaction was then performed with addition of 20–1000 μL of

1 mM $AuCl_4^-$ in distilled water to an aqueous solution of the as-synthesized dAgNPs to obtain Au−Ag bimetallic nanostructures (Figure 1). We observed clear color change from yellow of dAgNPs solution to red, blue, or purple of dextran-coated hollow Au−Ag nanoparticles (dHANs) with different colors depending on the amount of added $AuCl_4^-$ within several seconds at room temperature (dHAN1−7; higher numbers indicate addition of larger volumes of the $AuCl_4^-$ solution). No further color change was observed after 10 s, implying that the reaction completed within only 10 s. We think that the galvanic replacement reaction was much faster under very mild conditions in our system compared to conventional methods due to the presence of the dextran coating on the surface of AgNPs. For the progression of galvanic replacement reaction of the sacrificial silver core precursor, the dissolved $AuCl_4^-$ in aqueous solvent must be desolvated. At this stage, the layer of dextran on the silver surface could increase the local concentration of Au ions at the surface and desolvation could be facilitated with its abundant hydroxyl groups by directly interacting with Au ions. Therefore, galvanic replacement reaction could proceed faster while maintaining structural stability compared to AgNPs omitting dextran coating.

UV−vis spectra of dAgNPs showed an SPR band at 420 nm, which red-shifted to the NIR region toward 900 nm in wavelength upon addition of $AuCl_4^-$, indicating structural changes of nanoparticles due to galvanic replacement of dAgNPs to dHANs (Figure 2). TEM images and elemental mapping by high-angle annular dark-field scanning transmission electron microscopy/energy-dispersive spectrometry (HAADF-STEM/EDS) showed the hollow spherical nanostructure and the formation of Au−Ag bimetallic core nanostructures with a surface dextran shell of ∼5 nm thickness in dHAN1−3 (Figure 2 and Supporting Information Figure S1). In the TEM images of dHAN4−7, the presence of the dextran shell is not clearly discernible. However, dextran should exist either outside or inside the nanoparticle clusters to hold small nanoparticles together, to yield separately well-dispersed clusters of spherical particles with irregular size without dissociation from each other as seen in the TEM images. Absorption peak at ∼530 nm in UV−vis spectra of dHAN6−7 also supported the formation of individual gold nanoparticles in multibranched nanostructures (Figure 2). In addition, the existence of surface dextran coating was indirectly confirmed by excellent colloidal stability of dHAN1−7 at high temperature, salt, acidic, and basic pH values and biological buffer solution (Supporting Information Figures S2−S6). Without any surface coating, Au or Ag nanoparticles cannot maintain good colloidal stability under such harsh conditions. Taken together, dextran coating in the dAgNP not only accelerated the galvanic replacement reaction but also

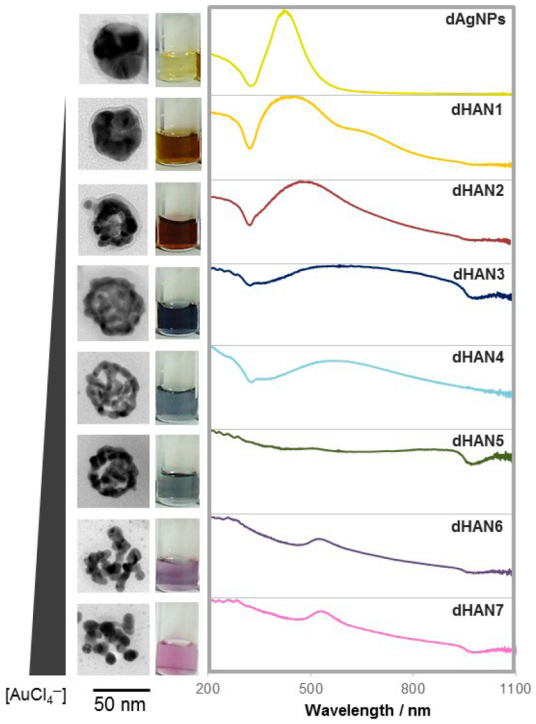

Figure 2. TEM images (left), photograph images (middle), and UV−vis absorption spectra (right) of the prepared dHANs; top to bottom, dAgNPs and dHAN1−7. TEM images showed changes in shapes of the prepared nanostructures depending on the concentration of the added $AuCl_4^-$. Photograph images represented differences in color change depending on the concentration of $AuCl_4^-$ used for galvanic replacement reaction. UV−vis absorption spectra showed a red shift to the near-IR region as more galvanic replacement reaction occurred (dHAN1−dHAN4). Characteristic absorption peaks corresponding to AuNPs were observed at a wavelength of ∼530 nm when the shell structure collapsed and clusters of small AuNPs were generated (dHAN6,7).

served as a structural support during the deformation process to maintain structural stability of Au−Ag bimetallic clusters. Additionally, hydrophilic and biocompatible dextran coating makes the dHANs more attractive and suitable for various bioapplications (Supporting Information Figure S7).

Recent reports on alcohol and glucose oxidation by AuNPs emphasized the advantages of ambient reaction with dissolved oxygen and acceleration by oxygen purging. We expected that hydroxyl groups of dextran coating on dHANs could be readily oxidized if the Au−Ag nanostructure serves as a catalyst for alcohol oxidation. First, catalytic reduction of 4-nitrophenol by $NaBH_4$, a model reaction which is catalyzed by Ag, Au, and Cu nanoparticles, was carried out by using the dHANs as a catalyst to check its catalytic activity. In this model reaction, metal surface lowers the kinetic barrier of the electron transfer from BH_4^- to 4-nitrophenol. Absorbance at 400 nm corresponding to 4-nitrophenolate ions formed by the addition of $NaBH_4$ rapidly diminished in the presence of dHAN1−7. Specifically, dHAN3 induced decrease of the absorption peak of

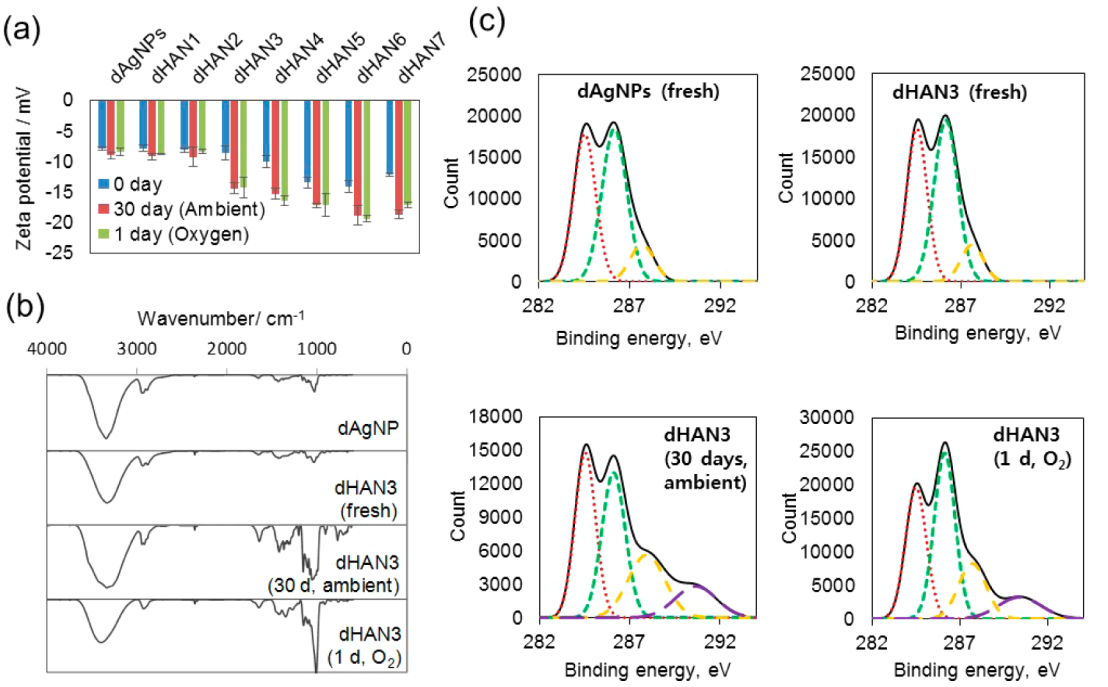

Figure 3. Characterization of the oxidation of the surface dextran *via* self-catalytic behavior of the core Au−Ag nanoparticle. (a) Zeta-potential measurement of dAgNP and dHAN1−7 before and after oxidation by ambient atmospheric exposure for 30 days and oxygen purging for 1 day. Both oxidation methods similarly induced more negative zeta-potential values of the dHAN1−7 compared to freshly synthesized particles. (b) IR spectra supported the presence of more abundant carbonyl groups on the dHAN3 after the oxidation reaction. (c) XPS data showed the presence of the oxidized functional groups such as aldehyde, ketone, and carboxylic acid after the self-catalytic oxidation reaction by showing the measured binding energy of C−C bond (284.5 eV, red), −C−OH bond (hydroxyl; 286.5 eV, green), −C═O bond (aldehyde/ketone; 287.9 eV, yellow), and O═C−OH bond (290.6 eV, violet).

4-nitrophenolate down to 10% within 3 min. All as-synthesized dHANs showed much higher catalytic activity than control groups consisting of citrate-stabilized AgNPs and AuNPs, dAgNPs and dAuNPs. The result indicates that dextran coating does not impair catalytic activity of the core metal surface or the diffusion of compounds into the metal surface of the particles (Figure S8). We think that high catalytic activity of dHANs was due to a large surface area with porous structure of the hollow Au−Ag particles having catalytically active (111) facets, observed by HR-TEM image and FFT analysis (Figure S9).

Since the catalytic activity of the dHANs was validated, we thought that hydroxyl groups of dextran coating could be oxidized by a catalytically active Au−Ag core. We refer to this reaction as "intraparticle self-catalytic oxidation". To the best of our knowledge, there is no report on intraparticle self-catalytic reaction of surface-coated polymers on the gold nanomaterials to date. We carried out the oxidation reaction through two different approaches, long atmospheric exposure under ambient condition for a month and relatively short exposure with oxygen purging for a day. Under these oxidation conditions, zeta-potentials of dHANs decreased to more negative values, indicating formation of more negatively charged moieties on the surface (Figure 3a). We selected dHAN3 for further characterization of the self-catalytic oxidation and demonstration of chemo-thermotherapy due to the relatively intact hollow shell structure and the most significant changes in zeta-potentials before and after the oxidation reaction. Fourier transform infrared spectroscopy (FT-IR) analysis of hydroxyl (−OH; 3300 cm^{-1}, strong, broad) and carbonyl (−C═O; 1650 and 1710 cm^{-1}, aldehyde/ketone and carboxylic acid, respectively) supported the oxidation of surface dextran. Intensity ratio of carbonyl (1650 cm^{-1}) *versus* hydroxyl (3300 cm^{-1}) peaks dramatically increased after oxidation—0.060, 0.085, 0.248, and 0.231 for fresh dAgNPs, fresh dHAN3, dHAN3 after 30 day exposure to air, and dHAN3 after 1 day of oxygen purging, respectively (Figure 3b). Additionally, X-ray photoelectron spectroscopy (XPS) analysis of oxidized dHAN3 (C 1s) showed new peaks corresponding to aldehyde/ketone and carboxylic acid (290 and 292 eV, respectively), which were absent in the dHANs before oxidation (Figure 3c). Taken together, it was confirmed that the Au−Ag bimetallic nanoparticle core catalyzed oxidation of their surrounding hydroxyl-rich dextran coating, resulting in the introduction of carbonyl groups by catalytic transformation of hydroxyl to aldehyde/ketone and carboxylic acids. Importantly, the carbonyl group can serve as a convenient molecular handle for bioconjugation by forming a Schiff base with amines. Facilitated cleavage of Schiff base linkages under acidic environment has been considered as one useful

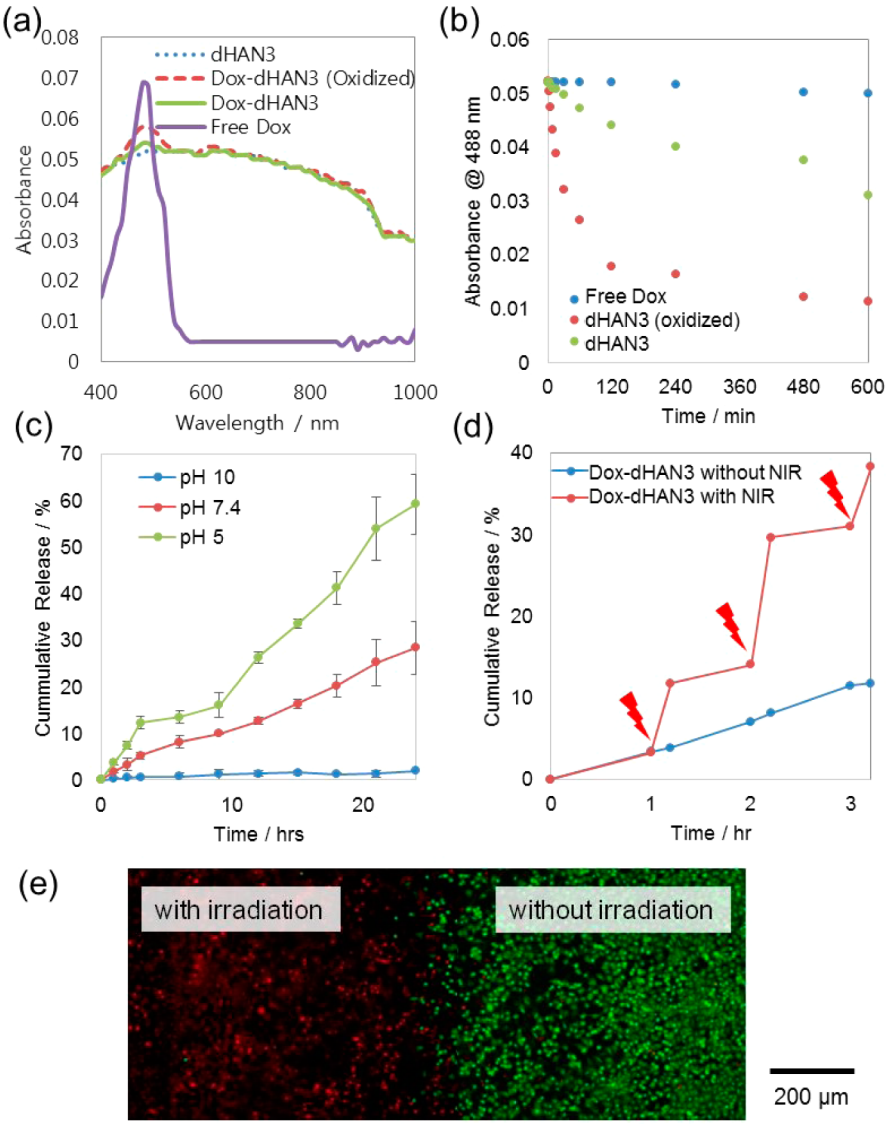

Figure 4. Dox loading and release profile of dHAN3 and hyperthermia effect of the Dox-loaded dHAN3. (a) Absorption spectra of the Dox-loaded dHAN3 showed absorbance at 488 nm corresponding to Dox. (b) Loading profile of Dox to dHAN3 was investigated by measuring absorption spectra of the supernatant of the mixed solutions of Dox and dHAN3 over time. Amount of the loaded Dox was estimated as 35 000 Dox per oxidized dHAN3 particle and 20 000 Dox per nonoxidized dHAN3 particle. (c) Dox release profile of the Dox-dHAN3 was examined under acidic, neutral, and basic pH condition without any irradiation. No Dox was released in a pH 10 buffer solution, but gradual release of Dox was observed at pH 7.4 and pH 5. Faster release of Dox at lower pH could be due to more favorable breakage of the imine bond at acidic pH. (d) Release of Dox from dHAN3 induced by 808 nm NIR irradiation was observed in pH 5 buffer solution. Three times of NIR irradiation at 1, 2, and 3 h led to about four times higher Dox release overall, indicating expedited Dox release due to hyperthermic effect of the dHAN3. (e) Combination of photothermic effect and Dox of the Dox-loaded dHAN3 induced highly efficient and selective HeLa cell death, as shown in live/dead staining (green, live cells; red, dead cells) after Dox-dHAN3 treatment, followed by NIR irradiation at designated area.

strategy for controlled drug release.[40] These properties suggested the high potential of our dHANs in the development of controlled drug release system.

We next demonstrate anticancer drug delivery system using dHANs and Dox as a model drug. Dox was loaded to dHAN3 by simply mixing the oxidized dHAN3 with Dox solution at room temperature. UV−vis absorption spectra revealed that ∼35 000 Dox molecules were loaded per particle (Figure 4a). Loading capacity of nonoxidized dHAN3 was ∼20 000 Dox per particle, which was lower than that of the oxidized dHAN3 (Figure 4b). We think that higher Dox loading capacity of the dHANs after oxidation originates from the Schiff-base-mediated Dox conjugation to the oxidized dextran. It is also possible that the Dox conjugation to the surface of dHANs provided a hydrophobic environment around the nanoparticle surface, which could be favorable for recruiting more Dox molecules near the dHANs and, thus, promoting further loading of Dox inside the hollow space of the dHANs. Next, release of the loaded Dox was observed for 24 h at three different pH values—acidic (pH 5.0), neutral (pH 7.4), and basic (pH 10.0) conditions by measuring UV−vis absorption of Dox at 488 nm of the supernatant after precipitating

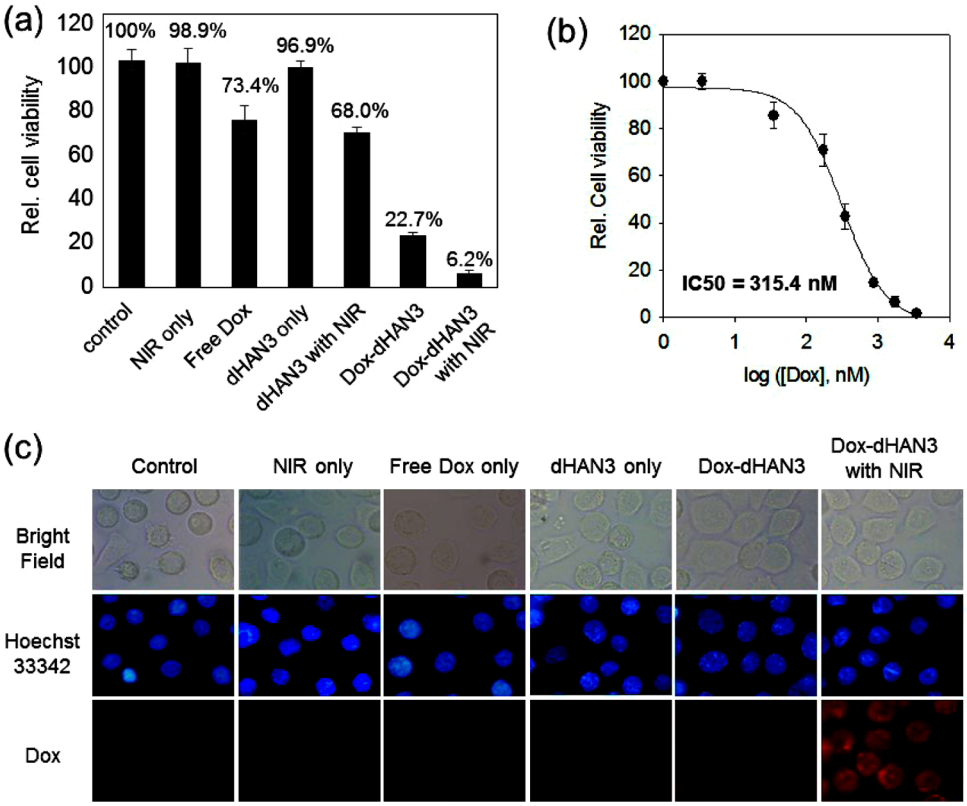

Figure 5. Quantitative viability assay of HeLa cells treated with Dox-dHAN3. (a) Dox-loaded dHAN3 induced decrease in cell viability down to 22.7%, and additional NIR irradiation expedited cell death down to 6.2% of viability. As controls, cells treated with NIR irradiation only or dHAN3 only did not show notable decrease in viability. Free Dox treatment and dHAN3 treatment with NIR irradiation decreased HeLa cell viability only down to 73.4 and 68.0%, respectively. (b) IC_{50} value of the Dox-dHAN3 with NIR against HeLa cells was measured as 315.4 nM, which is notably lower than the reported IC_{50} value of free Dox, ~1 μM. (c) Fluorescence images of HeLa cells showed that NIR irradiation induced Dox release from the internalized Dox-dHAN3 by showing Dox signals localized inside nuclei.

dHANs (Figure 4c). At pH 10, the loaded Dox was hardly released even after 24 h but the loaded Dox was released up to ~20% for 24 h with linear increase over time at pH 7.4. At pH 5.0, much faster release of Dox was observed with the cumulative release of about 60% of the loaded Dox over 24 h because Schiff base linkage is expected to be cleaved under acidic environment.

We next observed the temperature change of an aqueous solution of the dHANs upon irradiation using a 808 nm NIR laser. The dHANs showed light absorption at broad range of wavelength including 808 nm. Temperature of the 100 pM dHAN3 increased from 25.2 to 41.2 °C upon NIR irradiation (0.4 W/cm^2, 2 min), whereas temperature of PBS control solution was increased only 1.6 °C after the same treatment. This high temperature elevation is known to be sufficient to induce target cell death or to release loaded drugs (Figure S10).[41] Figure 4d shows the Dox release profile from the Dox-loaded dHAN3 with or without stimulation by NIR light irradiation. The dHAN3 was repeatedly irradiated over a period of 6 min, followed by 54 min of intervals without NIR irradiation during a total of 3 h 10 min. The NIR irradiation induced burst Dox release from the dHAN3, but the nonirradiated control group showed spontaneous release with a gradual slope. HeLa cells were next treated with the Dox-dHAN3, followed by the NIR irradiation (10.2 W/cm^2, 8 min) at designated region. Live/dead cell staining revealed that nearly 100% cell death was induced after treatment with the Dox-dHAN3 and subsequent irradiation (Figure 4e).

Before quantitative investigation of the therapeutic efficacy of the chemo-thermo treatment, the cytotoxicity of the dHAN3 itself toward HeLa cells was first evaluated by MTT assay and live/dead staining. MTT assay showed that more than 60% of cells were viable even at the highest concentration of dHAN3 (200 pM) we could practically use due to high viscosity of dHAN3 suspension (Figure S11). In the present study for chemo-thermotherapy, we typically used 50 pM of the dHAN3, which ensured more than 90% of cell viability and high colloidal stability in serum-containing cell culture media.

Next, the efficacy of chemo-thermotherapy was quantitatively evaluated by using dHAN3 (50 pM) loaded with Dox (1.75 μM). Significant reduction in cell viability was observed down to 6.2% after 808 nm NIR irradiation (7 W/cm^2, 5 min) to the Dox-dHAN3 treated cells, whereas the Dox-dHAN3 treatment without irradiation decreased cell viability only down to 22.7% (Figure 5a). Neither only dHAN3 treatment nor the NIR irradiation induced notable cytotoxicity.

The dHAN3-omitting Dox lowered the cell viability to 68.0% upon the NIR irradiation. The cells treated with only Dox (1.75 μM) showed 73.4% of viability. Next, the chemo-thermotherapeutic effect of Dox-dHAN3 on HeLa cells was quantitatively measured with various concentrations of the Dox-dHAN3 ([Dox] = 3.5 nM to 3.5 μM) and subsequent NIR irradiation. IC_{50} value was measured as 315.4 nM, which is considerably lower than the previously reported value of free Dox ($\sim$1 μM) (Figure 5b). We next observed HeLa cells by fluorescence microscopy after Hoechst 33342 nuclear staining. Fluorescence intensity corresponding to Dox in the HeLa cells treated with Dox-dHANs and NIR irradiation was much higher than that in the cells treated with Dox only or Dox-dHANs without irradiation (Figure 5c). Collectively, combination of photothermal effect derived by the irradiation of Dox-dHAN3 and subsequent acceleration of Dox release would explain high efficacy of the Dox-loaded dHAN3 as cancer therapeutics.

CONCLUSION

In conclusion, dextran-coated hollow Au–Ag bimetallic nanostructures were prepared by fast galvanic replacement reaction and employed as a combinational chemo-thermotherapeutic tool. In the present study, the dextran layer played multiple important roles: (i) to expedite the galvanic replacement reaction; (ii) to maintain structural integrity of nanostructures by preventing structural collapse; (iii) to endow excellent colloidal stability of the prepared nanostructures under even harsh conditions and good biocompatibility with low cytotoxicity; and (iv) to allow facile introduction of carbonyl groups for further bioconjugation on the dHANs *via* intraparticle catalytic oxidation of hydroxyl group. We also demonstrated highly efficient chemo-thermotherapy by the Dox-loaded dHAN3, which was achieved by combination of (i) high payload of Dox outside and inside of dHANs, (ii) hyperthermia by NIR irradiation, and (iii) the controlled Dox release *via* photothermic effect induced by NIR irradiation. We think that simple preparation of a biocompatible, robust hollow Au–Ag nanostructure and its straightforward surface modification, high drug payload, and hyperthermic effect will endow highly versatile applicability as a multifunctional nanostructure platform.

METHODS

Materials. Hydrogen tetrachloroaurate(III) hydrate was purchased from Kojima Chemicals Co. (Sayama, Saitama, Japan). 3-(4,5-Dimethylthiazol-2-yl)-2,5-diphenyl tetrazolium bromide (MTT), silver nitrate, and doxorubicin were purchased from Sigma (St. Louis, MO, USA). Sodium borohydride was purchased from Aldrich (Milwaukee, WI, USA). Hydrochloric acid was purchased from Samchun (Seoul, Korea). Dextran from leuconostoc spp. ($M_r \sim 15000-25000$) was purchased from Fluka (Milwaukee, WI, USA). Trisodium citrate dehydrate and sodium hydroxide were purchased from Junsei (Tokyo, Japan). Phosphate-buffered saline (PBS, 10×), Dulbecco's modified Eagle's medium (DMEM), and fetal bovine serum (FBS) were purchased from WelGENE (Seoul, Korea). Live/dead viability/cytotoxicity assay kit and Hoechst 33342 were purchased from Molecular Probes Invitrogen (Carlsbad, CA, USA). Amicon ultracentrifuge filter device (cutoff: 100 kDa) was purchased from Millipore (Billerica, MA, USA). Minisart RC25 syringe filters (0.20 and 0.45 μm pore size) were purchased from Sartorius stedim biotech (Goettingen, Germany). All chemicals were used as received.

Synthesis of Citrate-Stabilized AuNPs, dAgNPs, and dHANs. *Synthesis of 50 nm Sized Citrate-Stabilized AuNPs.* The 50 mL of 0.25 mM hydrogen tetrachloroaurate(III) solution was heated to boil, and 300 μL of 34 mM trisodium citrate dehydrate solution was then added. The reaction mixtures were boiled for 20 min until the color changed to red and then cooled to room temperature. The final product was kept at 4 °C until use.

Synthesis of dAgNPs. Dextran (12.0 g) was dissolved in distilled water (160 mL, 18.2 MΩ) to prepare 7.5 wt % solution. The prepared dextran solution was heated until boiling, and 864 μL of 250 mM silver nitrate stock solution was added to make 50 nm sized dAgNPs. The reaction mixture was boiled for 30 min until the color of the mixture turned deep yellow. The reaction mixture was then cooled to room temperature. The product was rinsed with distilled water four times using Amicon ultra filter (cutoff: 100 kDa). The product was further purified by passing the mixture through 0.45 and 0.20 μm pore sized syringe filters. Finally, dAgNPs were redispersed in 8 mL of distilled water and stored at 4 °C.

Preparation of dHANs by Galvanic Replacement Reaction. To 1 mL of the prepared dAgNPs was added 4 mL of distilled water and briefly inverted several times for thorough mixing. Next, dHANs were prepared by addition of 20 μL (dHAN1)/50 μL (dHAN2)/100 μL (dHAN3)/150 μL (dHAN4)/250 μL (dHAN5)/500 μL (dHAN6)/1000 μL (dHAN7) of 1 mM hydrogen tetrachloroaurate(III) hydrate stock to the dAgNPs. After addition of Au(III) solution, the mixed solution was simply shaken for 10 s, followed by purification using an Amicon ultracentrifuge filter (cutoff: 100 kDa) with distilled water. The final product was characterized by UV–vis spectrophotometry and kept at 4 °C.

Characterization of the Prepared dHANs. Energy-filtering transmission electron microscope LIBRA 120 (Carl Zeiss, Germany), high-resolution TEM, and HAADF-STEM Tecnai F20 (FEI, Netherlands) were used to obtain images of dHANs. UV–vis spectrophotometer S-3100 (Scinco, Korea) and SynergyMx (Biotek, UK) were used to obtain UV–vis absorption spectra. Zeta-potential measurement was carried out by using a Zetasizer Nano ZS90 (Malvern, UK). X-ray photoelectron spectroscopy was obtained by AXIS-His (KRATOS, NY, USA). Energy-dispersive spectroscopy was carried out by using EDAX (NJ, USA). Then, 808 nm NIR irradiation was performed by surgical laser accessories OCLA (Soodogroup Co., Korea). Cell images were taken using a Ti-inverted fluorescence microscope equipped with a 60× (1.4 numerical aperture) objective (Nikon Co., Japan) and a CoolSNAP cf charge-coupled device (CCD) camera (Photometrics, Tucson, AZ, USA) and BX51 M optical microscope (Olympus Co., Japan) equipped with fluorescence light source and filters.

Catalytic Reaction. *4-Nitrophenol Reduction.* The catalytic activity of the cit-Ag, cit-Au, dAgNPs, dAgNPs, and dHANs was tested by using 4-nitrophenol as a substrate for reduction to 4-aminophenol. One milliliter of 120 μM 4-nitrophenol solution was mixed with 2 mL of 0.1 M freshly prepared $NaBH_4$ solution in a standard cubic quartz cell. In this reaction, 4-nitrophenol oxidized to 4-nitrophenolate ion by $NaBH_4$ and color changed from pale yellow to deep yellow. After the measurement of initial absorbance at 290 and 400 nm, 10 μL of 200 pM each nanoparticle solution was added to the reaction mixture in a quartz cell. The catalytic activity was determined by observing the decrease in the absorbance at 400 nm over time.

Characterization of Photothermal Effect. *Temperature Elevation Measurement.* To verify the temperature elevation by photothermal

conversion, 20 μL of dHAN was dropped onto a piranha-cleaned silicon plate. The 808 nm NIR laser was irradiated to the droplet on the plate with intensity of 0.4 W/cm^2 for 2 min, and the temperature change was measured by a thermogun.

Cell-Based Hyperthermia Measurement. To examine hyperthermia by photothermal conversion, dHAN3 in 1× PBS was treated to HeLa cells in a 6-well plate that was seeded with confluency of 50 000 cells/well. After 4 h of incubation in a humidified 5% CO_2 incubator at 37 °C, residual dHAN3 was removed and washed with 1× PBS, followed by replacing with serum-containing media. Next, the cells were irradiated with an 808 nm NIR laser with an intensity of 10.2 W/cm^2 for 8 min at ambient condition and incubated for 2 h. Following incubation, 50 μL (96-well) or 200 μL (6-well) of the combined live/dead cell staining solution (2 μM calcein AM and 4 μM EthiD-1 in D-PBS) was added to each well and incubated for 30 min for staining. Fluorescent images of the cells were obtained using an inverted microscope equipped with fluorescence light source and filters.

Measurement of Doxorubicin Loading Efficiency and Release Profile. *Dox Loading to dHAN3 and Oxidized dHAN3.* Free Dox solution (1 mM) in distilled water was added into the dHAN3 and the oxidized dHAN3 suspension, and the mixture was gently shaken at room temperature for 10 h. After incubation, the Dox-loaded dHANs were precipitated by centrifugation at 13 000 rpm for 10 min, and the supernatant was transferred to Eppendorf tubes. The precipitate was rinsed with pH 10 buffer solution to prevent imine bond breakage, and all the supernatant was collected. The amount of Dox dissolved in the gathered supernatant was estimated by measuring absorbance at 488 nm ($\varepsilon_{Dox,488}$ = 11 500 L mol^{-1} cm^{-1}) based on Beer's law. Dox loading capacity of the dHAN3 and the oxidized dHAN3 was then estimated by calculating the difference between the initially added Dox amount and the unloaded Dox remained in supernatant.

$$\text{loaded Dox} = \frac{\text{Dox}_{\text{initial}} - \text{Dox}_{\text{unloaded}}}{\text{dHANs}}$$

$$[\varepsilon_{Dox,488} = 11500\ \text{L mol}^{-1}\ \text{cm}^{-1}]$$

Dox Release Profile at Different pH with or without NIR Irradiation. To monitor the release of the loaded Dox at various pH values, the Dox-dHAN3 was dispersed in citrate buffer (pH 5.0), phosphate-buffered saline (pH 7.4), and Tris-HCl buffer (pH 10.0) solution at room temperature. At designated time points, the solution of Dox-dHAN3 was centrifuged at 13 000 rpm for 5 min to pull down the nanoparticles, and the amount of the released Dox was determined by measuring absorbance of supernatant at 488 nm. The measurement was repeated every 3 h for 24 h. NIR irradiation triggered Dox release was carried out by an 808 nm laser irradiation at 7 W/cm^2 for 6 min. The Dox-dHAN3 solution was centrifuged at 13 000 rpm for 5 min, and supernatants were collected. The concentration of the released Dox in the supernatant was determined by measuring absorbance at 488 nm before and after irradiation.

Cellular Uptake. *Fluorescence and Dark-Field Image.* The Dox-loaded dHAN3 in 1× PBS was treated to cultured HeLa cells with a density of 50 000 cells per well in a 6-well culture plate. After the treatment, the cells were incubated for 4 h in a humidified 5% CO_2 incubator at 37 °C. Residual Dox-dHAN3 was removed and washed with 1× PBS followed by replacing with fresh serum-containing media. The cells were irradiated with an 808 nm NIR laser for controlled release of Dox and then incubated for another 1 h. Cell nucleus was stained by Hoechst 33342, and cells were observed under a fluorescence microscope.

Cell Viability Assay. *Cell Culture.* HeLa cells were maintained in Dulbecco's modified Eagle's medium (DMEM) containing 4.5 g/L D-glucose, supplemented with 10% FBS (fetal bovine serum), 100 units/mL penicillin, and 100 μg/mL streptomycin. The cells were grown in a humidified 5% CO_2 incubator at 37 °C.

MTT Assay for Cell Viability Measurement. MTT (3-(4,5-dimethylthiazol-2-yl)-2,5-diphenyl tetrazolium bromide) powder was dissolved in 1× PBS at 5 mg/mL concentrations and filtered through a 0.2 μm pore sized sterilized syringe filter. The stock solution was stored at 4 °C. HeLa cells were seeded with a density of 10 000 cells per well of a 96-well culture plate with 100 μL of growth media (about 50−70% confluency). After cells were treated with dHAN3, Dox-dHAN3, and Dox-dHAN3 with or without NIR irradiation, the cells were incubated for 24 h at 37 °C. Then, the cells were rinsed with 1× PBS. Twenty microliter MTT stock solution was added to detect the metabolically active cells, and the cells were incubated for 2−4 h until a purple color developed. The media were discarded, and 200 μL of DMSO was added to each well to solubilize water-insoluble formazan salt. Then, the optical densities of each well in the plates were measured at 560 nm. Mean and standard deviation of triplicates were calculated and plotted.

Live/Dead Cell Staining. The cytotoxicity and hyperthermia effect of dHAN3 were investigated by using the live/dead viability/cytotoxicity assay kit. HeLa cells were seeded at 10 000 cells per well of a 96-well cell culture plate and 50 000 cells per well of a 6-well cell culture plate. The cells were incubated with dHAN3 at designated concentrations in 1× PBS for 4 h, then replaced with fresh media and incubated for 20 h. Following incubation, 50 μL (96-well) or 200 μL (6 well) of the live/dead cell staining solution (2 μM calcein AM and 4 μM EthiD-1 in D-PBS) was added to each well and incubated for 30 min. Images were obtained using a microscope equipped with fluorescence light source and filters.

Conflict of Interest: The authors declare no competing financial interest.

Acknowledgment. This work was supported by the Basic Science Research Program (2011-0017356) and by the Research Center Program (EM1202) of IBS (Institute for Basic Science) through the National Research Foundation of Korea (NRF) funded by the Korean government (MEST).

Supporting Information Available: Analytical data available free of charge *via* the Internet at http://pubs.acs.org.

REFERENCES AND NOTES

1. Liu, S.; Liu, J.; Han, X.; Cui, Y.; Wang, W. Electrochemical DNA Biosensor Fabrication with Hollow Gold Nanospheres Modified Electrode and Its Enhancement in DNA Immobilization and Hybridization. *Biosens. Bioelectron.* **2010**, *25*, 1640–1645.
2. Hirsch, L. R.; Jackson, J. B.; Lee, A.; Halas, N. J.; West, J. L. A Whole Blood Immunoassay Using Gold Nanoshells. *Anal. Chem.* **2003**, *75*, 2377–2381.
3. Oldenberg, S. J.; Westcott, S. L.; Averitt, R. D.; Halas, N. J. Surface Enhanced Raman Scattering in the Near Infrared Using Metal Nanoshell Substrates. *J. Chem. Phys.* **1999**, *111*, 4729–4735.
4. Jackson, J. B.; Westcott, S. L.; Hirsch, L. R.; West, J. L.; Halas, N. J. Controlling the Surface Enhanced Raman Effect *via* the Nanoshell Geometry. *Appl. Phys. Lett.* **2003**, *82*, 257–259.
5. Corma, A.; Garcia, H. Supported Gold Nanoparticles as Catalysts for Organic Reactions. *Chem. Soc. Rev.* **2008**, *37*, 2096–2126.
6. Haruta, M. Gold as a Novel Catalyst in the 21st Century: Preparation, Working Mechanism and Applications. *Gold Bull.* **2004**, *37*, 27–36.
7. Melancon, M. R.; Lu, W.; Yang, Z.; Zhang, R.; Cheng, Z.; Elliot, A. M.; Stafford, J.; Olson, T.; Zhang, J. Z.; Li, C. *In Vitro* and *In Vivo* Targeting of Hollow Gold Nanoshells Directed at Epidermal Growth Factor Receptor for Photothermal Ablation Therapy. *Mol. Cancer Ther.* **2008**, *6*, 1730–1739.
8. Sershen, S. R.; Westcott, S. L.; Halas, N. J.; West, J. L. Temperature-Sensitive Polymer-Nanoshell Composites for Photothermally Modulated Drug Delivery. *J. Biomed. Mater. Res.* **2000**, *51*, 293–298.
9. You, J.; Zhang, G.; Li, C. Exceptionally High Payload of Doxorubicin in Hollow Gold Nanospheres for Near-Infrared Light-Triggered Drug Release. *ACS Nano* **2010**, *4*, 1033–1041.
10. El-Sayed, M. A. Some Interesting Properties of Metals Confined in Time and Nanometer Space of Different Shapes. *Acc. Chem. Res.* **2001**, *34*, 257–264.
11. Cepak, V. M.; Martin, C. R. Preparation and Stability of Template-Synthesized Metal Nanorod Sols in Organic Solvents. *J. Phys. Chem. B* **1998**, *102*, 9985–9990.

12. Murphy, C. J.; Jana, N. R. Controlling the Aspect Ratio of Inorganic Nanorods and Nanowires. *Adv. Mater.* **2002**, *14*, 80–82.
13. Jin, R.; Cao, Y.; Mirkin, C. A.; Kelly, K. L.; Schatz, G. C.; Zheng, J. G. Photoinduced Conversion of Silver Nanospheres to Nanoprisms. *Science* **2001**, *294*, 1901–1903.
14. Chen, J.; Wiley, B.; Li, Z. Y.; Campbell, D.; Saeki, F.; Cang, H.; Au, L.; Lee, J.; Li, X.; Xia, Y. Gold Nanocages: Engineering Their Structure for Biomedical Applications. *Adv. Mater.* **2005**, *17*, 2255–2261.
15. Landsman, M. L.; Kwant, G.; Mook, G. A.; Zijlstra, W. G. Light-Absorbing Properties, Stability, and Spectral Stabilization of Indocyanine Green. *J. Appl. Physiol.* **1976**, *40*, 575–583.
16. Chen, W. R.; Adams, R. L.; Bartels, K. E.; Nordquist, R. E. Chromophore-Enhanced *In Vivo* Tumor Cell Destruction Using an 808-nm Diode Laser. *Cancer Lett.* **1995**, *94*, 125–131.
17. Lu, W.; Xiong, C.; Zhang, G.; Huang, Q.; Zhang, R.; Zhang, J. Z.; Chun, L. Targeted Photothermal Ablation of Murine Melanomas with Melanocyte-Stimulating Hormone Analog-Conjugated Hollow Gold Nanospheres. *Clin. Cancer Res.* **2009**, *15*, 876–886.
18. Kennedy, L. C.; Bickford, L. R.; Lewinski, N. A.; Couqhlin, A. J.; Hu, Y.; Day, E. S.; West, J. L.; Drezek, R. A. A New Era for Cancer Treatment: Gold-Nanoparticle-Mediated Thermal Therapies. *Small* **2011**, *7*, 169–183.
19. Weissleder, R. A Clearer Vision for *In Vivo* Imaging. *Nat. Biotechnol.* **2001**, *19*, 316–317.
20. Helmchen, F.; Denk, W. Deep Tissue Two-Photon Microscopy. *Nat. Methods* **2005**, *2*, 932–940.
21. Anderson, R. R.; Parrish, J. A. Selective Photothermolysis: Precise Microsurgery by Selective Absorption of Pulsed Radiation. *Science* **1983**, *220*, 524–527.
22. Haruta, M.; Yamada, N.; Kobayashi, T.; Iijima, S. Gold Catalysts Prepared by Coprecipitation for Low-Temperature Oxidation of Hydrogen and of Carbon Monoxide. *J. Catal.* **1989**, *115*, 301–309.
23. Pina, C. D.; Falletta, E.; Prati, L.; Rossi, M. Selective Oxidation Using Gold. *Chem. Soc. Rev.* **2008**, *37*, 2077–2095.
24. Hayashi, T.; Inagaki, T.; Itayama, N.; Baba, H. Selective Oxidation of Alcohol over Supported Gold Catalysts: Methyl Glycolate Formation from Ethylene Glycol and Methanol. *Catal. Today* **2006**, *117*, 210–213.
25. Hashimi, A. S. K.; Hutchings, G. J. Gold Catalysis. *Angew. Chem., Int. Ed.* **2006**, *45*, 7896–7936.
26. Gorin, D. J.; Toste, D. Relativistic Effects in Homogeneous Gold Catalysis. *Nature* **2007**, *446*, 396–403.
27. Prati, L.; Porta, F. Oxidation of Alcohols and Sugar Using Ac/C Catalysts: Part 1. Alcohols. *Appl. Catal. A: Gen.* **2005**, *291*, 199–203.
28. Mertens, P. G. N.; Bulut, M.; Gevers, L. E. M.; Vankelecom, I. F. J.; Jacobs, P. A.; De Vos, D. E. Catalytic Oxidation of 1,2-Diols to Hydroxy-Carboxylates with Stabilized Gold Nanocolloids Combined with a Membrane-Based Catalyst Separation. *Catal. Lett.* **2005**, *102*, 57–61.
29. Abad, A.; Almela, C.; Corma, A.; Garcia, H. Unique Gold Chemoselectivity for the Aerobic Oxidation of Allylic Alcohols. *Chem. Commun.* **2006**, *30*, 3178–3180.
30. Comotti, M.; Pina, C. D.; Matarrese, R.; Rossi, M. The Catalytic Activity of "Naked" Gold Particles. *Angew. Chem., Int. Ed.* **2004**, *43*, 5812–5815.
31. Sun, Y.; Mayers, B. T.; Xia, Y. Template-Engaged Replacement Reaction: A One-Step Approach to the Large-Scale Synthesis of Metal Nanostructures with Hollow Interiors. *Nano Lett.* **2002**, *2*, 481–485.
32. Mulvaney, P.; Giersig, M.; Ung, T.; Liz-Marzan, L. M.; Mulvaney, P. Direct Observation of Chemical Reactions in Silica-Coated Gold and Silver Nanoparticles. *Adv. Mater.* **1997**, *9*, 570–575.
33. Zhong, Z.; Yin, Y.; Gates, B.; Xia, Y. Preparation of Mesoscale Hollow Spheres of TiO_2 and SnO_2 by Templating against Crystalline Arrays of Polystyrene Beads. *Adv. Mater.* **2000**, *12*, 206–209.
34. Oldenburg, S. J.; Averitt, R. D.; Westcott, S. L.; Halas, N. J. Nanoengineering of Optical Resonances. *Chem. Phys. Lett.* **1998**, *288*, 243–247.
35. Hwang, L.; Zhao, G.; Zhang, P.; Rosi, N. L. Size-Controlled Peptide-Directed Synthesis of Hollow Spherical Gold Nanoparticle Superstructures. *Small* **2011**, *7*, 1939–1942.
36. Ji, T.; Lirtsman, V. G.; Avny, Y.; Davidov, D. Preparation, Characterization, and Application of Au-Shell/Polystyrene Beads and Au-Shell/Magnetic Beads. *Adv. Mater.* **2001**, *13*, 1253–1256.
37. Huang, X.; Neretina, S.; El-Sayed, M. A. Gold Nanorods: From Synthesis and Properties to Biological and Biomedical Applications. *Adv. Mater.* **2009**, *21*, 4880–4910.
38. Weast, R. *CRC Handbook of Chemistry and Physics*, 62nd ed.; CRC Press: Boca Raton, FL, 1981.
39. Jang, H.; Kim, Y.-K.; Ryoo, S.-R.; Kim, M.-H.; Min, D.-H. Facile Synthesis of Robust and Biocompatible Gold Nanoparticles. *Chem. Commun.* **2010**, *46*, 583–585.
40. Kratz, F.; Beyer, U.; Schutte, M. T. Drug-Polymer Conjugates Containing Acid-Cleavable Bonds. *Crit. Rev. Ther. Drug Carrier Syst.* **1999**, *16*, 245–288.
41. Halperin, E. C.; Perez, C. A.; Brady, L. W.; Wazer, D. E.; Freeman, C.; Prosnitz, L. R. *Perez and Brady's Principles and Practice of Radiation Oncology*, 5th ed.; Lippincott Williams & Wilkins: Philadelphia, 2007; p 637.